

# The inverse-Compton X-ray-emitting lobes of the high-redshift giant radio galaxy 6C 0905+39

M. C. Erlund,<sup>1\*</sup> A. C. Fabian<sup>1</sup> and Katherine M. Blundell.<sup>2</sup>

<sup>1</sup>*Institute of Astronomy, Madingley Road, Cambridge CB3 0HA*

<sup>2</sup>*University of Oxford, Astrophysics, Keble Road, Oxford OX1 3RH*

31 October 2018

## ABSTRACT

We present new *XMM-Newton* data of the high-redshift ( $z = 1.883$ ), Mpc-sized giant radio galaxy 6C 0905+39. The larger collecting area and longer observation time for our new data means that we can better characterise the extended X-ray emission, in particular its spectrum, which arises from cosmic microwave background photons scattered into the X-ray band by the energetic electrons in the spent synchrotron plasma of the (largely) radio-quiet lobes of 6C 0905+39. We calculate the energy that its jet-ejected plasma has dumped into its surroundings in the last  $3 \times 10^7$  years and discuss the impact that similar, or even more extreme, examples of spent, radio-quiet lobes would have on their surroundings. Interestingly, there is an indication that the emission from the hotspots is softer than the rest of the extended emission and the core, implying it is due to synchrotron emission. We confirm our previous detection of the low-energy turnover in the eastern hotspot of 6C 0905+39.

## 1 INTRODUCTION

At redshift  $z = 1.88$ , 6C 0905+39 is one of the highest redshift giant radio galaxies known. It spans 111 arcsec on the sky (Law-Green et al. 1995), which represents a projected size of 945 kpc in the cosmology assumed in this paper. Blundell et al. (2006) observed this powerful, classical double FR II (Fanaroff & Riley 1974) radio galaxy with *Chandra* and detected extended X-ray emission along the axis of the radio source which we concluded was emitted by inverse-Compton scattering of the Cosmic Microwave Background (ICCMB, CMB) by the lobes (undetected in the radio) of the radio galaxy. The sheer physical size of the source means that the extended emission cannot be due to up-scattering of a nuclear photon component and the breadth of the X-ray lobes rules out jet emission via beamed ICCMB. It is common for the lobes of radio sources at low- and high-redshift to emit X-rays in this way (e.g. Croston et al. 2005, Overzier et al. 2005, Erlund et al. 2006). Higher redshift objects are easier to detect and/or less ambiguous than low-redshift objects because IC-CMB is not redshift-dimmed compared with other emission processes (Schwartz 2002). The energy stored in ICCMB-scattering electrons can potentially be considerable and is more representative of the actual amount of energy that a radio source pumps into its environment than synchrotron radio emission because it is much longer lived and probes the lower Lorentz-factor electrons thought to dominate typical particle energy distributions.

In this paper we present recent *XMM-Newton* observations of 6C 0905+39. Throughout this paper, all errors are quoted at  $1\sigma$  unless otherwise stated and the assumed cosmology is  $H_0 = 71 \text{ km s}^{-1} \text{ Mpc}^{-1}$ ,  $\Omega_0 = 1$  and  $\Omega_\Lambda = 0.73$ . One arcsecond represents 8.518 kpc on the plane of the sky at the redshift ( $z =$

$1.883 \pm 0.003$ ) of 6C 0905+39 and the Galactic absorption along the line-of-sight is  $1.91 \times 10^{20} \text{ cm}^{-2}$  (Dickey & Lockman 1990).

## 2 DATA REDUCTION

Our *XMM-Newton* data of 6C 0905+39 consists of 58.0 ks of EPIC-pn data and 61.9 ks of data for each of the EPIC-MOS cameras. 6C 0905+39 was observed on 2006 October 30. The standard pipeline was used to reduce the data, SAS tools EPCHAIN and EMCHAIN were used for the EPIC-pn and both EPIC-MOS data respectively. After filtering the resulting files to remove periods dominated by flares and taking dead-time intervals into account, 42.2 ks of good-time for the PN, and 53.1 ks for both MOS 1 and MOS 2 were left. In total, in the 0.2 – 8 keV band (after summing the MOS 1, MOS 2 and the PN data and using the regions shown in Fig 3), there are 1271 counts (of which 579 are background) in the source, 830 (422 background) in the extended emission (lobes and hotspots) and 441 counts (159 background) in the core. Spectra for the extended X-ray emission (excluding the 15 arcsec core region), the nucleus (15 arcsec circle) and background (an area of sky free from sources near 6C 0905+39 on the same chip) were extracted separately for each instrument. They were then stacked and fitted using *XSPEC* v 11.3.2. All spectral data were fitted over the 0.5 – 10 keV band. The nucleus of 6C 0905+39 is addressed in Erlund et al. (2008) and so is not discussed further here.

The radio data used in this paper first appeared in Blundell et al. (2006) and were reduced using standard AIPS techniques.

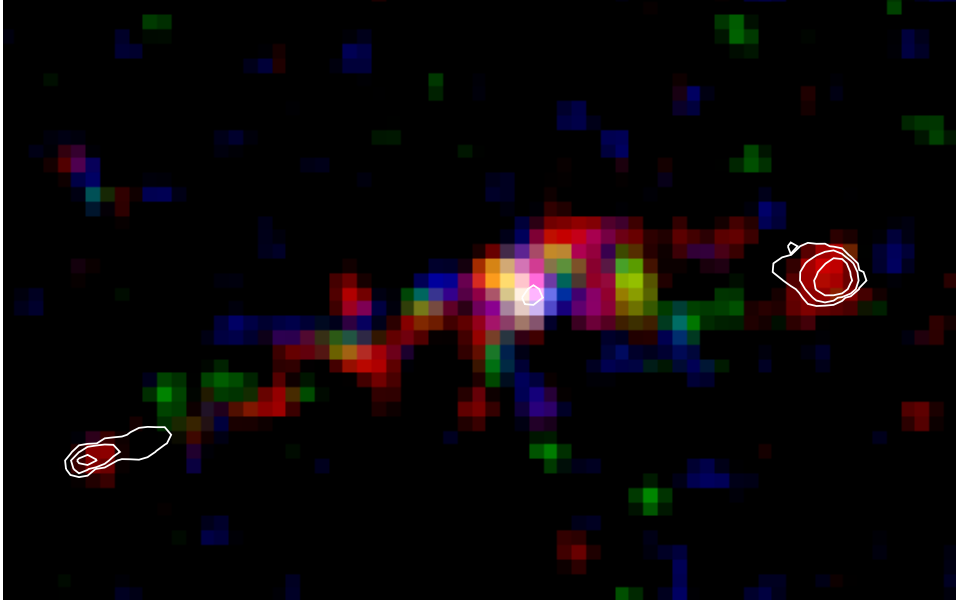


**Figure 1.** Image of our *XMM-Newton* data ( $132'' \times 83''$  with 2 arcsec pixels; the image has been smoothed by a Gaussian with  $\sigma$  of 2 pixels, the core of 6C 0905+39 is located at RA 09h08m16.9s, Dec +39d43m26s in J2000). The three colours represent soft (0.2 – 1 keV band; red), medium (1 – 3 keV band; green) and hard (3 – 10 keV band; blue) X-ray bands. Overlaid in white are VLA A-array 1.425-GHz radio contours (0.4, 1.7 and 7 mJy/beam). The X-ray emission from the hotspots is softer than the lobes and core and so they appear red.

### 3 RESULTS

Our *XMM-Newton* data clearly show X-ray emission extending along the radio axis of 6C 0905+39 to the east and west (Fig. 1). This was first detected by *Chandra* and presented in Blundell et al. (2006) where we noted that, as *Chandra* resolves the transverse extent of this extended emission ( $\sim 40$  kpc, although the paucity of counts makes the difficult to measure this accurately), it cannot be jet emission (since this would be very narrow) but rather is due to inverse-Compton up-scattering of the CMB by spent radio plasma from the lobes. The *XMM-Newton* data supports this interpretation. The spectra extracted from the EPIC-pn, MOS 1 and MOS 2 data were binned by 20 counts per bin and associated with a background spectrum, response and ancillary response files using GRPPHA. They were then fitted with a Galactic-absorbed power-law using XSPEC (which subtracts the background) giving a photon index of  $\Gamma = 1.61^{+0.19}_{-0.17}$  and a normalisation of  $1.9^{+0.2}_{-0.2} \times 10^{-6}$  ct keV $^{-1}$  cm $^{-2}$  s $^{-1}$  with a reduced-chi-squared of  $\chi^2_{\nu} = 0.98$  with 31 degrees of freedom (d.o.f.). The absorption-corrected X-ray luminosity of the extended emission in the 2 – 10 keV band is  $L_X = 1.5^{+0.1}_{-0.2} \times 10^{44}$  erg s $^{-1}$ , and the observed flux in the same band is  $F_X = 9^{+2}_{-2} \times 10^{-15}$  erg s $^{-1}$ . Blundell et al. (2006) found  $\Gamma = 2.7^{+1.7}_{-1.7}$  from the *Chandra* data, but the *XMM-Newton* spectra are better constrained and typical of extended inverse-Compton emission associated with radio galaxies (e.g. Croston et al. 2005; Erlund et al. 2006). (Note that the values presented for the extended emission in Erlund et al. 2008 came from a larger extraction region.)

The number of X-ray photons increases towards the core (by  $\sim 50$  per cent) as can be seen in Fig. 1 and Fig. 2. The latter figure shows four profiles: the eastern lobes in black; a source-free region in red to give an idea of the background level on the chip; the core in blue (i.e. roughly perpendicular to the radio axis); and a bright (comparison) source to the north-east of 6C 0905+39 which has been normalised so as the sides of the core profile are roughly

matched in green. This green line illustrates that the point spread function (PSF) of the central core does not significantly contaminate the extended emission. Each profile is calculated using a rectangular region 24 arcsec wide from a stacked 0.2 – 8 keV PN, MOS1 and MOS2 image with 7.7 arcsec pixels. The PSF is  $\sim 7.4$  arcsec at the FWHM which corresponds to one point.

Blundell et al. (2006) noted that most of the X-ray emission in the *Chandra* observation lay between the radio hotspots and core, along the lobes of 6C 0905+39. The more extended western hotspot emitted in X-rays but the eastern one did not at the upper limit of our *Chandra* observation. In Blundell et al. (2006), we interpreted the lack of X-ray emission from the eastern hotspot together with the presence of X-ray emission in the lobe material nearby as a direct detection of the low-energy turnover in the electron population ( $\gamma_{\min}$ ). Our deep *XMM-Newton* data show a very similar picture, with rather different X-ray emission associated with the eastern hotspot from that of the rest of the associated lobe. Interestingly, our new *XMM-Newton* observation reveals some very soft photons (approximately two thirds of these photons have energies below 0.8 keV) associated with the eastern hotspot, which would expect to be undetectable in our current *Chandra* observation. We consider the nature of this very soft emission in Section 4.0.2.

In order to determine whether there is any significant difference between the hardness ratio<sup>1</sup> of the X-ray emission from the hotspots, lobes and core, the number of counts in the regions shown in Fig. 3 were calculated for the PN and both MOS cameras in the soft and hard band (0.2 – 1 keV and 1 – 8 keV) respectively using CIAO tool *dmstat*. The counts in each region were calculated separately and by careful specification of the region files within *ds9* contamination of the core region in the lobe region was avoided.

<sup>1</sup> Here we calculate the hardness ratio,  $HR = \frac{H-S}{H+S}$ , where  $H$  is the number of counts in the hard band and  $S$  is the number of counts in the soft band

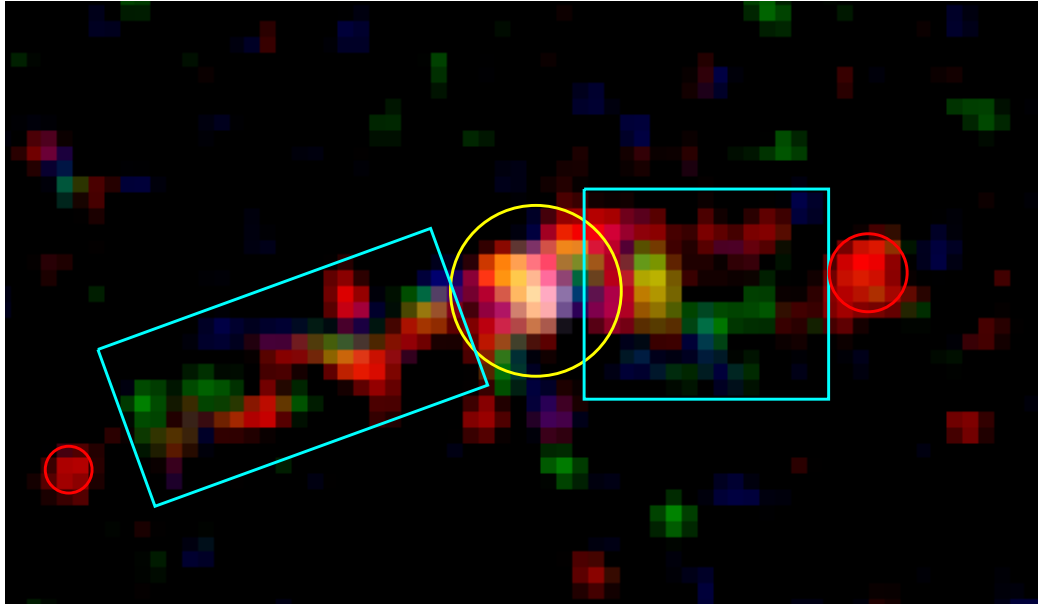


**Figure 3.** Three colour image ( $132'' \times 77''$ ; energy bands, pixels sizes and smoothing as in Fig. 1) illustrating the regions that were used when calculating the hardness ratio in the hotspots, lobes and core. The core region was excluded from the lobe regions. In Fig. 4, region 2 is the core region depicted here by a yellow circle, regions 1 and 3 are the lobe regions indicated as cyan rectangles and the hotspot regions, shown by small red circles, are regions 0 and 4. It can clearly be seen that the hotspot regions mainly contain soft (red) photons, in contrast with the other regions.

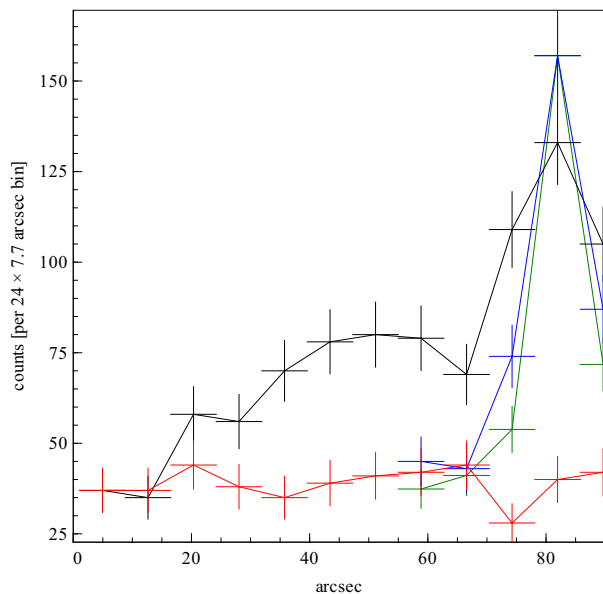


**Figure 2.** Profiles taken from the  $0.2 - 8$  keV mosaic of PN, MOS1 and MOS2 images. Each point represents a  $7.7 \times 24$  arcsec bin. The black line represents a profile along the eastern lobe of 6C 0905+39 only. The blue line is a profile going from north-east to south-west through the core. The red line represents a profile of a source-free region on the same chip. The green line represents a slice through a bright source to the north-east of 6C 0905+39, which has been normalised so that it matches the peak of the core profile.

These energy bands were chosen so that the number of counts in each band would be roughly equal. The hardness ratio in each region was calculated taking into account the background counts in each band. The resulting hardness ratio profiles as illustrated in Fig.

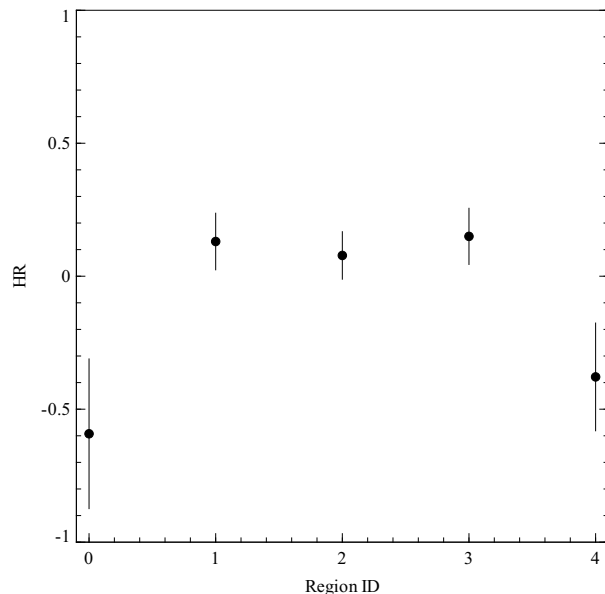


**Figure 4.** Hardness ratios calculated for the core (region 2); the two lobe regions (regions 1 and 3) and the two hotspot regions (regions 0 and 4), as illustrated in Fig. 3. The hardness ratio was calculated using the soft ( $0.2 - 1$  keV) and hard ( $1 - 8$  keV) bands. The error bars represent one standard deviation and are calculated using a Monte-Carlo simulation to propagate the errors on the two energy bands and due to the background. This plot shows that the hotspots are softer than the lobes and nucleus.

4, which shows that both hotspots are softer than the lobes and nucleus. A constant hardness ratio model is a poor fit to the data giving a best fit hardness ratio of 0.08 and a  $\chi^2_\nu = 2.6$ . Fig. 2 shows that the difference between the hardness ratio of the lobes and hotspots is unlikely to be due to contamination from the core.

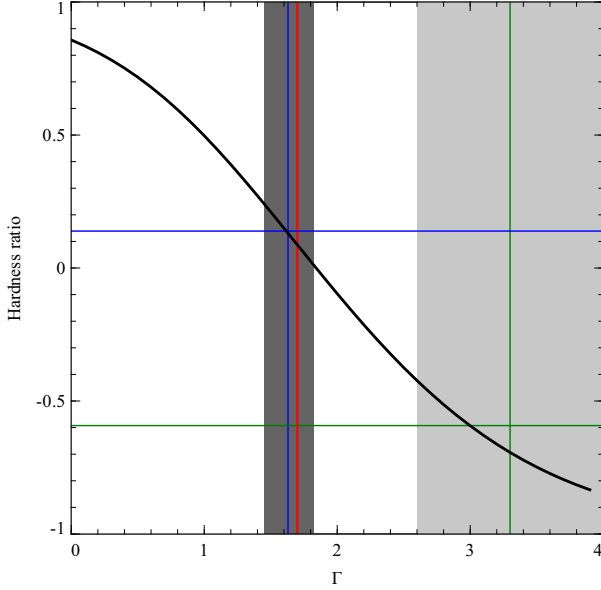


**Figure 5.** The thick solid black curve shows how hardness ratio (HR) varies as a function of photon index ( $\Gamma$ ). The green lines represent the measured hardness ratio and photon index (from spectral fitting) of the eastern hotspot region. The blue lines represent the same quantities for the lobe regions. The dark and light grey boxes represent the error on the photon index of the lobe and the eastern hotspot respectively from spectral fitting. The plot shows that the hardness ratio of the eastern hotspot in the X-ray is lower, so softer, than the radio hotspots. The thin red line represents the radio photon index considering the integrated flux density of the eastern radio hotspot and small radio emitting lobes together (calculated from values given in Law-Green et al. 1995 and shown outlined by white contours in Fig. 1).

The relationship between the X-ray photon index and hardness ratio is plotted in Fig. 5. *XSPEC* was used to evaluate this, taking into account the Galactic absorption along the line-of-sight to 6C 0905+39. Fig. 5 shows that lower hardness ratios imply steeper spectra. Thus at X-ray energies, the lobes have a flatter spectrum than the hotspots.

## 4 DISCUSSION

The diffuse X-ray emission spanning the gap between the core and the radio-emitting hotspots in 6C 0905+39 is a clear case of inverse-Compton scattering of CMB photons by the relativistic electrons stored in the spent synchrotron plasma once accelerated in the hotspot (as per the standard model of FR II radio galaxy evolution see e.g. Blundell et al. 1999). Beamed ICCMB emission from a relativistic jet can be ruled out from the morphology of the X-ray emission in the *Chandra* data which, at  $\sim 40$  kpc, is too laterally extended to correspond to a jet (Blundell et al. 2006).

### 4.0.1 The X-ray emission mechanism in the hotspots

The difference in the X-ray hardness ratio (and correspondingly the spectral index / photon index) between the hotspots and the lobes emission implies that different X-ray emission processes are taking place. Law-Green et al. (1995) studied the spectral indexes of the radio emission associated with the hotspots and the small amount

of lobe emission detected. The radio spectral indexes<sup>2</sup> of the eastern and western hotspots are  $\alpha = 0.8$  and  $1.0$  respectively, whereas the small radio lobes associated with these hotspots have spectral indexes of  $\alpha = 1.3$  and  $1.7$  respectively (these values come from Law-Green et al. 1995 who do not provide errors). In other words in the radio the spectral index may steepen from the hotspot to the lobe as would be expected from a curved particle distribution in a region with a magnetic field gradient (for reasons why this model is most likely see Blundell & Rawlings 2000). If it were the case that the X-rays from both the hotspot and lobes were from ICCMB emission, then the same curved spectrum and magnetic field should also cause the X-ray ICCMB emission to steepen between the hotspot and lobes (because the energy distribution will shift on expansion from the hotspot to the lobes). In fact the X-ray emission is steeper (i.e. softer) in the hotspot than in the lobes, this and the steepness of the spectrum implies that we are seeing the high energy tail of synchrotron emission in the hotspot.

Synchrotron self-Compton (SSC) emission has the same spectral shape as the synchrotron spectrum that has been up-scattered. The spectral indices of the radio hotspots are flatter than the X-ray spectral indices which would argue against this emission mechanism in the hotspot. However, to calculate the expected SSC flux in the eastern hotspot, we have assumed a minimum energy magnetic field with no low-energy cut-off ( $B_{\min} = 2.2 \times 10^{-5}$  G, for  $\gamma_{\min} = 1$ ), that the 408 MHz emission (107 mJy, peak and lobe flux; Law-Green et al. 1995) provides the SSC seed photon field and that the region responsible for up-scattering photons into the X-ray band is cylindrical with a diameter of 28 kpc and a length of 56 kpc. The predicted SSC 1 keV X-ray flux density is then  $7 \times 10^{-5}$  nJy. This is several orders of magnitude lower than what we actually detect, which is  $\sim 0.3$  nJy (calculated from a power-law fitted to the eastern and western hotspot where the normalisation between the two regions was independently fitted). However, Blundell et al. (2006) inferred a low-energy turnover of  $\gamma_{\min} \gtrsim 10^4$  in the population of this hotspot, in which case  $B_{\min} = 8.0 \times 10^{-6}$  G and the predicted 1 keV flux is  $3.8 \times 10^{-4}$  nJy. However, this would mean that the electrons emitting radio synchrotron lie below the low-energy turnover and so this emission mechanism can be ruled out (for confirmation of the detection of the low energy turnover in this object see Section 4.0.2).

Thus we conclude X-ray synchrotron emission from the hotspots, where the magnetic field strength is likely to be enhanced compared with that of the lobes and where particles are being accelerated, is the most likely explanation for the change in spectral index between the hotspot and the lobe emission. The 1 keV X-ray flux density is consistent with a cooling or curved synchrotron spectrum (see Fig. 6). Extrapolating the radio flux density at 408 MHz (107 mJy) up to 1 keV (assuming a straight power-law particle distribution) using the radio spectral index for the eastern hotspot ( $\alpha \sim 0.7$ , calculated from the integrated flux density values for the eastern hotspot-lobe component given in Law-Green et al. 1995) gives a predicted monochromatic X-ray flux density of  $\sim 80$  nJy; we detect  $\sim 0.3$  nJy, consistent with a steepening particle distribution curved in the usual way.

<sup>2</sup> The spectral index,  $\alpha$ , is related to the photon index,  $\Gamma$  as  $\alpha = \Gamma - 1$ ,  $\alpha$  is defined as  $S_\nu \propto \nu^{-\alpha}$ .

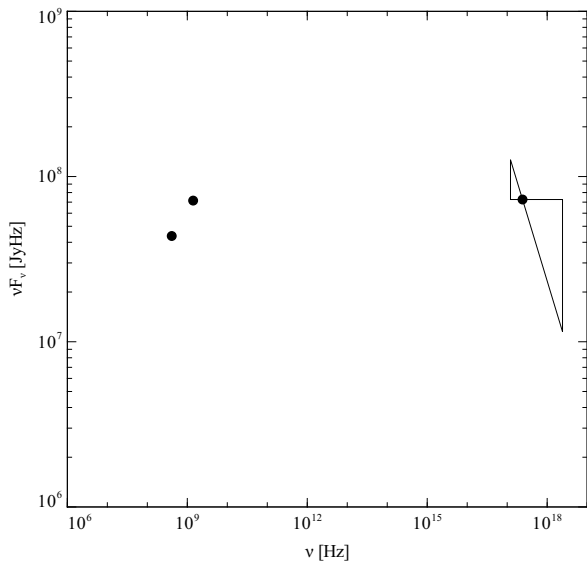


**Figure 6.** The SED of the eastern hotspot of 6C 0905+39 showing radio and X-ray data points. Radio points are integrated values for the eastern radio component (peak and lobes) and are taken from Law-Green et al. (1995). The spectral index calculated from these values between 408 MHz and 1.4 GHz is  $\alpha \sim 0.7$  which is slightly flatter than  $\alpha \sim 0.8$  quoted in Law-Green et al. (1995). The X-ray point is calculated from the normalisation of the eastern hotspot when the eastern and western hotspot are fitted together giving a normalisation of  $4.2_{-1.6}^{+2.0} \times 10^{-7}$  ct keV $^{-1}$  cm $^{-2}$  s $^{-1}$ . This gives a photon index of  $\Gamma = 2.4 \pm 0.4$  averaged over the eastern and western hotspot regions. This is a conservative measure of the steepness of the eastern hotspot as the harder component present in the western hotspot flattens the combined spectrum. However, it is better constrained than either the spectral fit of the eastern hotspot on its own or the photon index that we can infer from the hardness ratio of the eastern hotspot (see Fig. 4 and Fig. 5)

#### 4.0.2 The electron population in the hotspots

Noting the eastern hotspot of 6C 0905+39 to be inefficient at up-scattering CMB photons into the X-ray band, yet the nearby lobe to be efficient, Blundell et al. (2006) deduced that this was direct evidence of a low-energy turnover in the electron population. The morphology of our new *XMM-Newton* data is similar to that of our *Chandra* data.

Assuming a power-law electron distribution which extends back to low Lorentz factors ( $\gamma_{\min} \sim 1$ ), we make use of Equation 1 in Celotti & Fabian (2004) to determine the ratio of the predicted monochromatic X-ray luminosity,  $L_X$ , to monochromatic radio luminosity,  $L_R$  as follows

$$\frac{L_X}{L_R} = \frac{\mathcal{U}_{\text{CMB}}}{\mathcal{U}_B} \left( \frac{\nu_X \nu_B}{\nu_R \nu_{\text{CMB}}} \right)^{1-\alpha} (1+z)^{(3+\alpha)} \quad (1)$$

for the eastern hotspot, where  $\mathcal{U}_{\text{CMB}}$  is the energy density of the CMB at redshift  $z = 0$  and  $\mathcal{U}_B$  is the energy density of the magnetic field.  $\nu_X$ ,  $\nu_R$  and  $\nu_{\text{CMB}}$  are the observed frequencies in the radio and X-ray and the frequency of the peak of the CMB (again, at  $z = 0$ ) and  $\nu_B$  is the gyro-frequency.  $\alpha$  is the spectral index of the radio emission. Re-writing Equation 1 to express it as a function of

magnetic field strength,  $B$ , gives

$$\frac{L_X}{L_R} = 2^{2+\alpha} \pi^\alpha (1+z)^{3+\alpha} \mathcal{U}_{\text{CMB}} \left( \frac{e}{m_e c} \frac{\nu_X}{\nu_R \nu_{\text{CMB}}} \right)^{1-\alpha} B^{-(1+\alpha)} \quad (2)$$

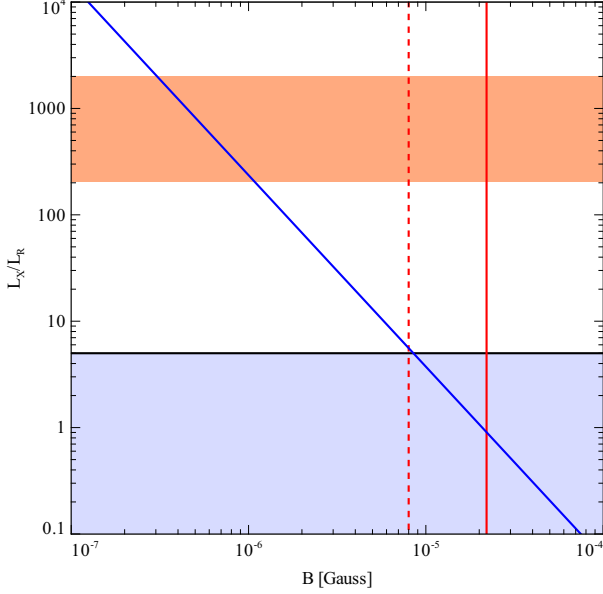
where  $e$  is the charge on the electron,  $m_e$  is the mass of the electron and  $c$  is the speed of light.

Fig. 7 shows the dependence of the X-ray–radio luminosity ratio on magnetic field strength at the redshift of 6C 0905+39: as the magnetic field decreases,  $\frac{L_X}{L_R}$  increases. In order to detect IC-CMB emission from the eastern hotspot, the magnetic field must be well below the minimum-energy magnetic field,  $B_{\min}$ , assuming no low-energy turnover. We note, however, that  $B_{\min}$  depends on  $\gamma_{\min}$ , with a higher  $\gamma_{\min}$  resulting in a lower  $B_{\min}$  (as described in Blundell et al. 2006 and illustrated in Fig. 7). It is therefore not possible to determine whether there is a low-energy turnover in the eastern hotspot using just our *XMM-Newton* and radio hotspot data so we now consider the other relevant information from these observations.

In Blundell et al. (2006) we considered the implications of the X-ray bright lobes and X-ray faint hotspots in 6C 0905+39. We concluded that the X-ray emission from the lobes implied that there must be a low-energy turnover in the eastern hotspot. The same argument still holds. Assuming a constant hotspot advancement speed (and that any expansion due to cooling takes place laterally), we can consider a region of lobe emission of the same length as the current eastern radio hotspot. The electrons responsible for inverse-Compton scattering CMB photons in the lobe have a Lorentz factor of  $\gamma \sim 10^3$ . These electrons will have cooled by at least an order of magnitude (Blundell et al. 1999) since they left the hotspot. So calculating the number of  $\gamma \sim 10^3$  electrons in a hotspot-sized region of the lobe tells us roughly the number of  $\gamma \sim 10^4$  electrons there must have been in the hotspot. We can therefore calculate the number of  $\gamma \sim 10^3$  electrons that there would be in the hotspot if there were no low-energy turnover, for an assumed spectral index. Then we calculate how much ICCMB emission these  $\gamma \sim 10^3$  electrons would have produced. The ratio between this and the radio emission at 408 MHz is shown as an orange region in Fig. 7 (the range of  $\frac{L_X}{L_R}$  reflects the uncertainty in the size of the hotspot region. We consider the lobe-length-to-hotspot-length ratio to be between 10 and 100.) Fig. 7 clearly shows that there must be a high low-energy turnover in the hotspot of 6C 0905+39 with a  $\gamma_{\min} \gtrsim 10^4$  as the expected 1 keV X-ray luminosity is two orders of magnitude above our detection limit.

Fig 7 implies that if we are seeing the low-energy turnover then the magnetic field in this hotspot must be relatively weak. This could explain why we see X-ray synchrotron hotspot emission from this source when usually high-luminosity FR II radio galaxies do not have high frequency synchrotron emission associated with their hotspots. This is thought to be because the magnetic field is too strong (see, for example, Meisenheimer et al. 1989 and Blundell et al. 1999).

We assume that power is transferred from the central black hole to the hotspots of 6C0905 along jets with high efficiency and with little radiation, presumably because most of the transferred energy is kinetic in the form of bulk motion of particles. Although a high bulk Lorentz factor  $\Gamma_b \sim 10$  could make radio through X-ray radiation from  $\gamma \sim 10^{3-5}$  particles in the jets undetectable by relativistic beaming, it would also greatly amplify the energy density of the CMB in the jet frame. This would lead to steep inverse-Compton losses of such energetic electrons, so electrons with these energies come from re-acceleration at the hotspots.



**Figure 7.** The plot shows the dependence of  $\frac{L_X}{L_R}$  on the magnetic field. If the very soft X-rays we detect in the eastern hotspot are due to synchrotron emission then this would provide a lower limit on the detectability of the 1 keV X-ray luminosity due to ICCMB (solid black line representing the observed 1 keV–408 MHz monochromatic luminosity ratio). Below this ratio, in the blue shaded region, the X-ray luminosity predicted would be undetectable. The solid blue line represents the predicted  $\frac{L_X}{L_R}$ , using the 408 MHz radio luminosity, as a function of  $B$ -field. The solid red line is the minimum energy magnetic field ( $B_{\min}$ ) in the eastern hotspot calculated assuming a cylindrical emission region with a diameter of 28 kpc and a length of 56 kpc, using the radio flux detected at 408 MHz and assuming  $\gamma_{\min} = 1$ . This intersects with the predicted  $\frac{L_X}{L_R}$  line in the undetectable region. Similarly, the dashed red line shows  $B_{\min}$  assuming  $\gamma_{\min} = 10^4$ . The orange region illustrates the range in  $\frac{L_X}{L_R}$  deduced from the X-ray bright lobe emission. The range in the orange region comes from the uncertainty in the length of the hotspot (here we estimate it to be between a tenth to a hundredth of the length of the lobe). This region lies well above the undetectable (blue shaded) region clearly showing that there must be a low-energy turnover, because the  $\gamma \sim 10^3$  electrons we would expect to find in the eastern hotspot are not there.

#### 4.0.3 Increase in X-ray lobe photons towards the core

There is a  $\sim 50$  per cent increase of X-ray emission towards the core (see Fig. 2; 30% of the total extended emission contaminates the core spectrum; see Erlund et al. 2008 for details). Given that the X-ray emission process is inverse-Compton, this implies that there are either more electrons with  $\gamma \sim 10^3$  or that the energy density of the seed photon field has increased.

The central galaxy is bright in the infra-red ( $\nu L_\nu \sim 4 \times 10^{44}$  erg s $^{-1}$ , at 5.8  $\mu\text{m}$ ; Seymour et al. 2007<sup>3</sup>) so will provide a source of photons which could be up-scattered (off lower Lorentz factor electrons,  $\gamma \leq 100$ ) along with the CMB (off  $\gamma \sim 10^3$  electrons); however, this photon field will be dominated by the CMB

beyond  $\sim 0.5$  arcsec of the central galaxy<sup>4</sup> and so can be ruled out.

The amount of ICCMB emission in the X-ray depends only on the number density of the electrons with  $\gamma \sim 10^3$  as the energy density of the CMB is constant throughout the source (and is independent of the magnetic field strength). One way in which there could be increasing numbers of  $\gamma \sim 10^3$  electrons closer to the core is if we are seeing the low-energy turnover in the electron population as the back-flowing plasma approaches the core and cools. There could be a contribution from more lobe plasma closer to the nucleus.

#### 4.0.4 Feedback

Emission that arises from inverse-Compton scattering of the CMB probes electrons with a lower energy than those typically responsible for producing radio synchrotron emission. In the case of 6C 0905+39, it means that the lobes of this high-redshift giant radio galaxy are detected in X-rays but not in the radio. Using the long-lived X-ray emission we can probe the amount of energy that 6C 0905+39 has pumped into its environment in the last  $\sim 3 \times 10^7$  yr,  $\mathcal{E}_e$ : approximately the length of time required to cool the electrons responsible for up-scattering the CMB into the X-ray band i.e those with Lorentz factors  $\gamma \sim 1000$ . We follow the arguments in Erlund et al. (2006) making use of their Equation 4:

$$\mathcal{E}_e = \frac{3}{4} \frac{L_X m_e c}{U_{\text{rad}} \gamma_e \sigma_T} \simeq \frac{3}{4} \frac{L_{44}}{\gamma_e (1+z)^4} 10^{64}, \quad (3)$$

where  $L_X$  is the X-ray luminosity in the 2–10 keV band and  $L_X = L_{44} \times 10^{44}$  erg s $^{-1}$ . The luminosity of the extended emission (both lobes and hotspots) emission is  $L_X = 1.5^{+0.1}_{-0.2} \times 10^{44}$  erg s $^{-1}$  in the 2–10 keV band, but there is a further  $L_X \sim 1.0 \times 10^{44}$  erg s $^{-1}$  contaminating the core spectrum (Erlund et al. 2008), meaning that the whole of the extended emission has a luminosity of  $L_X \sim 3 \times 10^{44}$  erg s $^{-1}$ .  $U_{\text{rad}}$  is the energy density of the photon field which is being up-scattered, in this case the CMB.  $\gamma_e$  is the Lorentz factor of the electrons responsible for most of the up-scattering: we assume that  $\gamma_e = 1000$ .  $\sigma_T$  is the Thomson cross-section. The lower limit to the amount of energy pumped into the environment by 6C 0905+39 is  $\sim 3 \times 10^{59}$  erg; including protons can increase this by two to three orders of magnitude to  $\sim 10^{62}$  erg or more.

Some clusters of galaxies require a large amount of energy deposited into the X-ray emitting gas to offset cooling and explain why significant amounts of cool gas are not detected in the X-ray in the centres of these systems. This feedback requires a power input of the order of  $L_{\text{feedback}} \sim 10^{44 \pm 1}$  erg s $^{-1}$  (Dunn & Fabian 2006) which gives a total energy of  $\mathcal{E}_{\text{feedback}} \sim 10^{59 \pm 1}$  erg over  $3 \times 10^7$  yr. This simple comparison is to illustrate the huge amount of energy stored in the lobes of powerful radio galaxies: enough to stem a cooling flow. Other powerful FR II radio sources have similar lower limits to their reservoirs of energy stored in electrons (i.e. Erlund et al. 2006). Most radio galaxies in clusters are FRI radio sources which are likely to be less powerful.

#### 4.0.5 Energy in ghost reservoirs

Saripalli et al. (2005) found four giant radio galaxies at  $z < 0.13$  in

<sup>3</sup> calculated using the flux density in the IRAC 5.8  $\mu\text{m}$  band

<sup>4</sup> The energy density of the photons is calculated using  $U_{\text{IR}} = \frac{L_{\text{IR}}}{\pi c R^2}$ , equating it to the energy density of the CMB which is  $\sim 3 \times 10^{-11}$  erg cm $^{-3}$  and solving for  $R$ , which is the distance from the nucleus in cm. The galaxy has been approximated as a point source.

a statistically complete survey using the 2100 deg<sup>2</sup> SUMSS field. None of these sources were classical double FR II radio galaxies. One is an FRI and the other three are also below the FRI–FR II luminosity divide but are possibly relic FR II sources because they have relaxed lobes and no hotspots (see also Cordey 1987 for another example of a large relic radio galaxy). This illustrates how rare sources such as 6C 0905+39 are at low redshifts. If three of Saripalli et al. (2005) relaxed doubles are in fact relic sources as they suggest, then powerful galaxies will be more common at higher redshift (closer to the peak in the space density of radio sources). 6C 0905+39 may be such an example as it has clear hotspots and, unlike its lower redshift counterparts, it has very little lobe emission at radio frequencies (Law-Green et al. 1995). The lack of radio lobe emission is due to a lack of particles having the right energies to radiate synchrotron emission at radio wavelengths, given the ambient magnetic field strength. (Radio observations at 408 MHz, Law-Green et al. 1995, and at 1.4 GHz, Blundell et al. 2006, appear not to have suffered from flux loss due to interferometric under-sampling, see Blundell et al. 2006.)

Sources such as the three relaxed doubles in the Saripalli et al. (2005) complete sample contain large reservoirs of aged synchrotron plasma which is ideally placed to up-scatter the CMB. These sources appear to be the most common sort of giant radio galaxy at low redshift based on the results in Saripalli et al. (2005) (they made up three out of four of the sources in their complete sample). Most giant radio galaxies could contribute to the anisotropies in the CMB and therefore are a potential contaminant in SZ (Sunyaev-Zel’dovich) surveys, particularly relic giant radio sources which are not strong radio emitters and so would be undetectable in the radio at relatively low redshifts. Given that most of the X-rays associated with 6C 0905+39 are associated with its extended emission, and are not co-spatial with the radio emission, this radio galaxy has pumped an otherwise completely undetectable  $\sim 3 \times 10^{59}$  erg into its environment.

## 5 CONCLUSIONS

Our *XMM-Newton* observation of the giant, high-redshift ( $z = 1.88$ ) radio galaxy 6C 0905+39 clearly shows extended X-ray emission aligned along the radio axis of the source. The longer observation time and greater sensitivity of our *XMM-Newton* observations means that we can better characterise this emission. It is richer than the previous *Chandra* data, with an increase in X-ray emission towards the central source and a difference in the hardness ratio of the hotspots and lobe emission. We demonstrate that the soft X-ray emission in the hotspots of 6C 0905+39 is most likely to be X-ray synchrotron emission. We confirm our previous detection of the low-energy turnover in the eastern hotspot and suggest that the increase in X-ray emission towards the core is due to the low-energy turnover in the electron population being revealed as the electron population cools.

We find that the minimum energy that 6C 0905+39 has pumped into its environment in the last  $\sim 3 \times 10^7$  yr is  $\sim 3 \times 10^{59}$  erg (protons could increase this by a factor of  $10^2 - 10^3$ ) and that it is clear that in 6C 0905+39, older plasma is more efficient at up-scattering the CMB than freshly accelerated plasma. This implies that there are more electrons with  $\gamma \sim 10^3$  in the older plasma and thus that the younger plasma has a low-energy turnover above  $\gamma_{\min} \sim 10^3$ .

The complete sample of Saripalli et al. (2005) of low-redshift giant radio galaxies shows that actively fed giant FR II sources are

rare (they found none), but that relic FR II sources may be the most common type of low-redshift giant radio galaxy (three out of four of their sources were potential relic sources). The Universe may be littered with the X-ray bright relics which could in their turn have an effect on the detected CMB anisotropies and hence SZ surveys. It is important to note that these would not be correlated with the observed distribution of currently radio-bright extended sources.

## ACKNOWLEDGEMENTS

MCE acknowledges STFC for financial support. ACF and KMB thank the Royal Society.

## REFERENCES

- Blundell K. M., Fabian A. C., Crawford C. S., Erlund M. C., Celotti A., 2006, *ApJ*, 644, L13
- Blundell K. M., Rawlings S., 2000, *AJ*, 119, 1111
- Blundell K. M., Rawlings S., Willott C. J., 1999, *AJ*, 117, 677
- Celotti A., Fabian A. C., 2004, *MNRAS*, 353, 523
- Cordey R. A., 1987, *MNRAS*, 227, 695
- Croston J. H., Hardcastle M. J., Harris D. E., Belsole E., Birkinshaw M., Worrall D. M., 2005, *ApJ*, 626, 733
- Dickey J. M., Lockman F. J., 1990, *ARA&A*, 28, 215
- Dunn R. J. H., Fabian A. C., 2006, *MNRAS*, 373, 959
- Erlund M. C., Fabian A. C., Blundell K. M., 2008, *MNRAS* accepted, 0
- Erlund M. C., Fabian A. C., Blundell K. M., Celotti A., Crawford C. S., 2006, *MNRAS*, 371, 29
- Fanaroff B. L., Riley J. M., 1974, *MNRAS*, 167, 31P
- Law-Green J. D. B., Eales S. A., Leahy J. P., Rawlings S., Lacy M., 1995, *MNRAS*, 277, 995
- Meisenheimer K., Roser H.-J., Hiltner P. R., Yates M. G., Longair M. S., Chini R., Perley R. A., 1989, *A&A*, 219, 63
- Overzier R. A., Harris D. E., Carilli C. L., Pentericci L., Röttgering H. J. A., Miley G. K., 2005, *A&A*, 433, 87
- Saripalli L., Hunstead R. W., Subrahmanyan R., Boyce E., 2005, *AJ*, 130, 896
- Schwartz D. A., 2002, *ApJ*, 569, L23
- Seymour N. et al., 2007, *ApJS*, 171, 353